A Magnetic Design Method Considering DC-Biased Magnetization for Integrated Magnetic Components Used in Multiphase Boost Converters

Jun Imaoka, *Member, IEEE*, Kenkichiro Okamoto, Shota Kimura, *Student Member, IEEE*, Mostafa Noah, *Student Member, IEEE*, Wilmar Martinez, *Member, IEEE*, Masayoshi Yamamoto, *Member, IEEE*, and Masahito Shoyama, *Senior Member, IEEE*

***Abstract*—High power density and high efficiency in dc/dc converters are required in various applications such as the automotive application. Interleaved multiphase circuits with integrated magnetic components can fulfill these requirements because passive components occupying significant space in power converters can be downsized without high-switching frequency driving of power devices. However, dc-biased magnetization is a drawback of integrated magnetic components because of unbalanced inductor average currents. This imbalance arises from the tolerance among the phase components. To overcome this problem, inductor average current control is implemented in interleaved multiphase dc/dc converters. Nevertheless, the imbalance cannot be completely eliminated because the current sensors inserted into each phase have gain errors. The purpose of this paper is to present a magnetic design method to improve the immunity to unbalanced currents. A comprehensive analysis is carried out with two main objectives: to prevent magnetic saturation, which may arise due to the current unbalance and to downsize the magnetic components by selecting the optimal coupling coefficient taking into consideration the maximum permissible percentage of unbalanced currents. Simulation case studies are presented to support the analysis. Finally, a 1-kW prototype of the interleaved boost converter is built to validate the accuracy of the design method.**

***Index Terms*—Boost converter, dc-biased magnetization, integrated magnetic components, interleaved converter, multiphase.**

I. Introduction

EFFORTS to achieve high power density and develop high-efficiency dc/dc converters are essential to improve the portability of power conversion systems and to conserve energy. In particular, the importance of power converters with their outstanding performance is growing along with the growth of the market in applications such as ecofriendly automotive industries [1]–[5], low-voltage and large-current voltage regulators for micro computer units [6]–[8], and renewable energies applications [9]–[10], among others. In addition, saving metal resources, including rare and base metals for magnetic components used in power converters, is a global concern [11]–[13].

Power converters are usually heavy and occupy significant space due to passive components such as inductors and capacitors that are used for energy storage. Therefore, downsizing of passive components is an effective way of achieving high power density for the entire converter. As a major solution method for downsizing passive components, high-switching frequency driving of power devices is a well-known technique. However, the disadvantage of this technique is that it leads to additional problems such as increased electromagnetic interference (EMI)/radio frequency interference noise or concentric thermal stress in active/passive devices. Therefore, many-sided solutions for high power density are required [14].

Interleaved multiphase circuit topologies have attracted attention as one of the solutions to fulfill these demands. In general, interleaved multiphase converters are switched with a 360°/PN (PN: number of phases) phase shift and the same duty ratio. The attractive features of interleaved multiphase converters are as follows.

1) This topology can downsize the output/input smoothing capacitors in comparison with single-phase converters, because the capacitance value and the effective current value flowing through the capacitors can be reduced by the alternating power transfer [4], [15].
2) This approach allows the input current to be shared among the phases. Therefore, power losses and thermal stress per active/passive devices can be reduced or distributed.
3) It is well known from the literature that multiphase topologies help to suppress EMI by increasing the number of phases in interleaved flyback converters [16], [17] or by changing the phase shift degree in interleaved boost power factor correction converters [17], [18].

The number of power devices and their drivers increase as a result of adapting multiphase topologies. However, these devices

Manuscript received October 24, 2016; revised January 17, 2017 and March 29, 2017; accepted May 11, 2017. Date of publication May 23, 2017; date of current version January 3, 2018. This work was supported by the Japan Society for the Promotion of Science KAKENHI Grant 16K18059. Recommended for publication by Associate Editor O. Lucia. *(Corresponding author: Jun Imaoka.)*

J. Imaoka, K. Okamoto, and M. Shoyama are with the Department of Electrical Engineering, Kyushu University, Fukuoka 819-0395, Japan (e-mail: imaoka@ees.kyushu-u.ac.jp; ie216662@ckt.ees.kyushu-u.ac.jp; shoyama@ees.kyushu-u.ac.jp).

S. Kimura and M. Noah are with the Department of Mechanical, Electrical and Electronic Engineering, Shimane University, Matsue 690-8504, Japan (e-mail: s159862@matsu.shimane-u.ac.jp; mosta.noah@gmail.com).

W. Martinez is with Toyota Technological Institute, Nagoya 468-8511, Japan (e-mail: whmartinezm@gmail.com).

M. Yamamoto is with the Institute of Materials and Systems for Sustainability, Nagoya University, Nagoya 464-8601, Japan (e-mail: m.yamamoto@imass.nagoya-u.ac.jp).

Color versions of one or more of the figures in this paper are available online at http://ieeexplore.ieee.org.

Digital Object Identifier 10.1109/TPEL.2017.2707385

can be packaged into multichip modules or intelligent power modules to reduce their mounting space, parasitic inductance, and resistance.

On the other hand, the number of magnetic components is similar to the number of parallel phases. Therefore, integrated magnetic components are used, whereby multiple windings can be installed on a single magnetic core. This integrated magnetic concept has been applied in both isolated and nonisolated dc/dc converters [3]–[5], [7]–[9], [19]–[22], [24]–[28]. The integrated magnetic components provide the following attractive features in interleaved multiphase boost converters.

1) DC fluxes generated by inductor average currents can be effectively canceled by the inversely coupling property. In addition, the peak-to-peak amplitude of the ac flux in a part of the magnetic core can be reduced. As a result, the downsizing of magnetic components can be realized.
2) Owing to mutual induction, inductor current ripple in each phase can be reduced. Consequently, the use of a small energy storage inductance for each phase is allowed. This is in contrast with the case of their discrete magnetic counterparts.
3) From a control-theory perspective, integrated magnetics improve the transient response speed because the inductor current slew rate is higher than that for noncoupled inductors [22]–[24].

Therefore, the use of interleaved multiphase circuit topology with integrated magnetic components results in outstanding performance for downsizing both the inductive and capacitive components.

Furthermore, in order to improve the performance of the integrated magnetic technique, magnetic core structures [5], [7]–[8], [25], applications of magnetic materials [3], winding arrangements [27], [28], and the derivation method for equivalent circuit models [29] have been discussed in detail.

In fact, in practical applications, there is a tolerance between the inductor currents in each phase, because of the inductor winding's uneven parasitic resistances, and on-resistances in the used power devices that are never exactly identical among the phases. In addition, a duty ratio difference between each switch may also affect the current imbalance. This current imbalance has two main negative outcomes: 1) A bigger value of the input/output capacitance is needed to compensate for the unbalanced power transfer, and 2) dc-biased magnetization occurs, which leads to a bigger magnetic core size to handle the undesirable flux.

One possible way of tackling the current imbalance in interleaved multiphase boost converters is to employ inductor average current controls. These control methods usually require inserting one current sensor per phase. Thus, the total number of current sensors equals the number of phases. These current sensors are usually connected in series with the inductors in each phase. However, it is practically difficult to completely eliminate the current imbalance because gain errors are introduced by the current sensors due to a difference of linearity, dc offsets, hysteresis, and sensitivity properties of the current sensors. Therefore, expensive high-precision current sensors or trained labor to adjust the gain of the sensors are needed. Hence, the large-scale production of these converters is difficult.

In order to overcome the aforementioned problems, inductor current measurement methods using a single-current sensor, connected in series with the smoothing capacitor [30] or to the dc-link part [31], [32], have been developed. The attractive features of these methods are that they not only reduce the current sensor's cost, volume, and weight, but also overcome the problem of gain mismatch between the current sensors. However, these methods also suffer from two disadvantages: First, the minimum and maximum duty cycles are limited [31], and second, setting the over-current protection becomes difficult because the inductor current cannot be measured directly. Therefore, considering the above-mentioned features, setting the current sensors in all phases is also an attractive option. Consequently, handling the dc-biased magnetization becomes a challenge, especially during the occurrence of small unbalanced inductor currents [33], [34].

This paper proposes a magnetic design method for integrated magnetic components considering the dc-biased magnetization when there are unbalanced inductor average currents. As a case study, this paper focuses on the two-phase interleaved boost converter with a loosely coupled inductor (LCI) using magnetic cores with three legs (EE or EI core shape). The features of the novel design method and the contributions of this paper are as follows.

1) With the purpose of improving the immunity to inductor average current unbalance, which may lead to magnetic saturation, the proposed method relies on inserting a small air gap in the transformer part of the LCI to increase the reluctance in order to minimize the effect of dc-biased magnetization.
2) However, inserting an air gap in the transformer part of the LCI will definitely decrease the value of the coupling coefficient. Consequently, lower coupling factors lead to a bigger magnetic core.
3) Based on (1) and (2), it is clear that there is a tradeoff between reducing the effect of dc-biased magnetization and downsizing the magnetic core.
4) This tradeoff is directly related to the coupling coefficient of the LCI. Therefore, the derivation for the optimal coupling coefficient is conducted to improve immunity to the unbalanced inductor average currents and to downsize of the magnetic components.

This paper is divided into six sections. Section II discusses the causes of the dc-biased magnetization of the LCI. The electromagnetic analysis is conducted in Section III, which is split into four subdivisions. The equations describing the peak flux in each leg is derived in Section III-A. The inductor ripple current equations are given in Section III-B. The relation between the peak flux and the inductor ripple current is described in Section III-C. In Section III-D, a comparison of the core volumes is conducted between the coupled and the noncoupled inductor, taking into consideration the maximum permissible percentage of unbalanced inductor average currents and based on the peak flux equations derived in the previous sections. Section IV presents the proposed design method, based on determining an optimal coupling coefficient to achieve peak

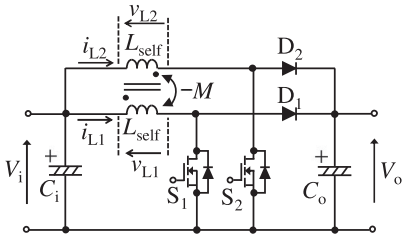

Fig. 1. Interleaved boost converter with a loosely coupled inductor.

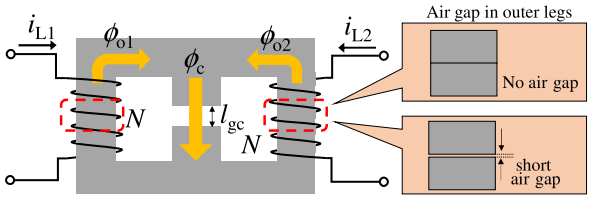

Fig. 2. Magnetic core structure of a loosely coupled inductor.

flux reduction. The proposed design method is supported by simulation and experimental results in Sections V-A and V-B, respectively. A comparison of the features of the proposed design method with other design methods is presented in Section V-C. Finally, the conclusion is presented in Section VI.

II. Causes of the DC-Biased Magnetization of Coupled Inductors

The circuit configuration of the interleaved boost converter with the LCI is shown in Fig. 1, where V_i and V_o are the input and output voltages, respectively; i_{L1} and i_{L2} are the inductor currents in each phase; S_1 and S_2 are the main switches; C_i and C_o are the input and output smoothing capacitance, respectively; D_1 and D_2 are the output diodes in each phase; L_{self} and M are the self-inductance and the mutual inductance of LCI with the same winding turns N, respectively. Fig. 2 shows the magnetic core structure of the LCI with EE or EI shape. The winding in each phase is inversely coupled with the other one in order to cancel the dc fluxes generated by the inductor average currents. Unbalanced conditions that adversely affect the circuit performance in Fig. 1 and their influence are considered as follows.

1) The duty ratio difference between S_1 and S_2 or the difference of parasitic resistance in each phase: these differences directly affect the difference between inductor average currents in each phase. However, by employing inductor average current controls, the average currents in each phase can be balanced by slightly modulating the duty ratio. The difference of duty ratio generated by average current controls is extremely small, hence the influence on the inductor current ripple and the peak-to-peak amplitude of ac flux are fairly small, respectively.
2) The difference between LCI's self-inductance in each phase: in this case, the difference between self-inductances in each phase is related to the difference between the leakage inductances in each phase if the number of turns in each phase is the same. Although the difference between the leakage inductances in each phase is naturally affected inductor ripple currents in each phase, this difference has to be paid attention from the flux density design point of view. This is because the leakage inductance of LCI is well known as the inductance related to dc flux [3], [5]. If flux density is regulated, LCI can be designed by setting an upper limit value of the leakage inductance.
3) Unbalanced average current condition: Unbalanced inductor average currents mainly affect dc-biased magnetization of the transformer part of LCI and this condition generates the undesirable flux. Even if inductor average current control is implemented, the current imbalance cannot be completely avoided as mentioned in Section I. Therefore, in this section, the causes of the dc-biased magnetization of LCI are described in detail.

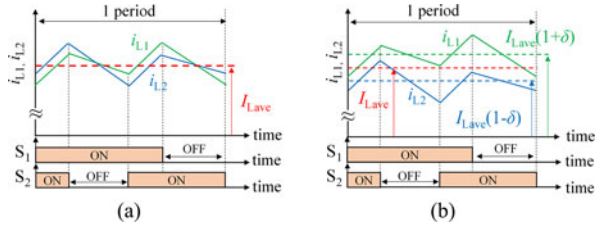

Fig. 3. Inductor current waveforms under the balanced and unbalanced conditions. (a) Balanced condition. (b) Unbalanced condition.

Fig. 3(a) and (b) shows the inductor current waveforms under balanced and unbalanced inductor current conditions, respectively. The inductor ripple current of LCI has a frequency equal to almost twice the switching frequency due to the effect of mutual induction. The inductor ripple current is composed of two current components: One is a common ripple current, which is equal to half of the input ripple current, and the other is a wheeling ripple current of the transformer [5], [8]. LCI has both the leakage inductances and the mutual inductance, and the inductances related to each current component are different. The current ripple analysis results are shown in Appendix I. In Fig. 3, I_{Lave} is the inductor average current in each phase, and $\delta(0 \le \delta < 1)$ is the maximum permissible percentage of unbalanced inductor average current. $\delta = 0$ means that the inductor average currents are completely balanced between the phases. In the same way, a higher δ means a large difference between the inductor average currents. If the input power P_i and input voltage V_i are not changed under both balanced and unbalanced conditions, the inductor average currents under the unbalanced condition can be represented as $I_{\mathrm{Lave}}(1+\delta)$, $I_{\mathrm{Lave}}(1-\delta)$ for phase one and phase two, respectively. This relationship can be shown as follows:

$$\begin{aligned} P_i &= V_i \cdot \{I_{\mathrm{Lave}}(1+\delta) + I_{\mathrm{Lave}}(1-\delta)\} \\ &= V_i \cdot 2I_{\mathrm{Lave}}. \end{aligned} \tag{1}$$

From this relationship, the unbalanced inductor average currents are symmetrically arranged around I_{Lave}. In the same way, Fig. 4(a) and (b) shows the dc flux behavior under balanced and unbalanced inductor average current conditions. For the balanced condition, as shown in Fig. 4(a), the dc fluxes in the outer legs are usually equal, and they circulate through the central leg, since the dc magnetomotive force (MMF) in each phase is the same.

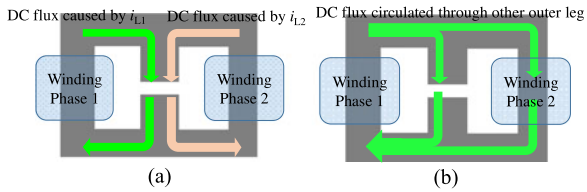

Fig. 4. DC flux behavior under the balanced and unbalanced average current conditions. (a) Balanced condition. (b) Unbalanced condition.

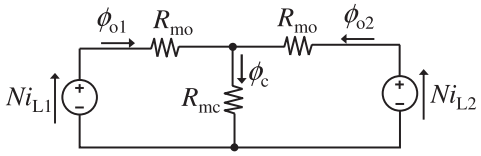

Fig. 5. Magnetic circuit model of LCI.

However, when there are unbalanced average currents flowing in the windings as shown in Fig. 4(b), the dc flux in the outer leg, where a higher average inductor current flows, becomes significantly high in comparison with the balanced condition. The main reasons are that the magnetic reluctance of the transformer part in the outer leg is low to improve the effect of mutual inductance, and the dc-MMF between each phase is different. Consequently, dc-biased magnetization occurs when there is a difference between the inductor average currents.

III. Characteristic Analysis Under the DC-Biased Magnetization

In this section, electromagnetic analysis is carried out considering the dc-biased magnetization phenomenon. This analysis provides guidelines for the proposed design method presented in Section IV. Essentially, a magnetic component is designed considering the maximum flux density by choosing the appropriate magnetic material and the core size in order to avoid magnetic saturation. The relationship between the maximum flux density $B_{\max}$, the maximum flux $\Phi_{\max}$, and the sectional area A_{core} of the core is given as follows:

$$\Phi_{\max} = B_{\max} \cdot A_{\text{core}}. \tag{2}$$

Therefore, $\Phi_{\max}$ is one of the key factors that influences the magnetic core size and volume because A_{core} size is influenced by $\Phi_{\max}$, and the magnetic design has to incorporate $B_{\max}$. Therefore, the peak flux analysis of the core relies on the magnetic circuit model of the LCI shown in Fig. 5, where R_{mo} and R_{mc} are the magnetic reluctances in the outer legs and the central leg of EE shape cores, respectively. ϕ_{o1}, ϕ_{o2}, and ϕ_c are the magnetic fluxes in the outer legs and the central leg. In this magnetic circuit model, the external leakage fluxes of the windings are neglected to simplify the analysis.

A. Magnetic Analysis of Peak Fluxes in Each Leg

In this section, the peak flux in the outer and central legs will be derived. First, dc fluxes are analyzed under the unbalanced inductor average current condition. The average inductor currents in each phase and dc fluxes in the outer leg and the central leg are denoted as $I_{\text{Lave}}(1+\delta)$, $I_{\text{Lave}}(1-\delta)$, Φ_{o1}, Φ_{o2}, and Φ_c, respectively. Based on the magnetic circuit model shown in Fig. 5, the following equations can be obtained:

$$\begin{cases} N \cdot I_{\text{Lave1}} = N \cdot I_{\text{Lave}}(1+\delta) = R_{\text{mo}} \cdot \Phi_{o1} + R_{\text{mc}} \cdot \Phi_c \\ N \cdot I_{\text{Lave2}} = N \cdot I_{\text{Lave}}(1-\delta) = R_{\text{mo}} \cdot \Phi_{o2} + R_{\text{mc}} \cdot \Phi_c \\ \Phi_c = \Phi_{o1} + \Phi_{o2}. \end{cases} \tag{3}$$

Thus, Φ_{o1}, Φ_{o2}, Φ_c, respectively, are

$$\begin{cases} \Phi_{o1} = N \cdot I_{\text{Lave}} \left(\dfrac{1}{R_{\text{mo}} + 2R_{\text{mc}}} + \dfrac{\delta}{R_{\text{mo}}} \right) \\ \Phi_{o2} = N \cdot I_{\text{Lave}} \left(\dfrac{1}{R_{\text{mo}} + 2R_{\text{mc}}} - \dfrac{\delta}{R_{\text{mo}}} \right) \\ \Phi_c = \dfrac{2 \cdot N \cdot I_{\text{Lave}}}{R_{\text{mo}} + 2R_{\text{mc}}}. \end{cases} \tag{4}$$

Then, the peak-to-peak amplitude of the ac flux in the outer leg is given by the following equation on the basis of Faraday's law:

$$\Phi_{\text{opp}} = \frac{V_i}{N} \cdot d \cdot T_s \tag{5}$$

where d and T_s are the duty ratios of the main switch and the switching period. On the other hand, the ac fluxes in the central leg are expressed as follows:

$$\begin{cases} \Phi_{\text{cpp\_d}\le 0.5} = \dfrac{1-2d}{1-d} \cdot \dfrac{V_i}{N} \cdot d \cdot T_s \\ \Phi_{\text{cpp\_d}>0.5} = \dfrac{2d-1}{d} \cdot \dfrac{V_i}{N} \cdot d \cdot T_s. \end{cases} \tag{6}$$

From (6), ac fluxes in the central leg depend on whether the duty ratio is less than or greater than 0.5. This is so because ac fluxes having 180° phase difference in the two outer legs are added at the central leg.

On the other hand, the higher peak flux in the outer leg, where the higher inductor average current flows, is shown by the following equation, considering that the peak flux is shown by the sum of the dc flux and half of the ac flux

$$\Phi_{\text{op}} = \Phi_o + \frac{1}{2}\Phi_{\text{opp}} = N \cdot I_{\text{Lave}} \cdot \left(\frac{1}{R_{\text{mo}} \cdot (1+2\alpha)} + \frac{\delta}{R_{\text{mo}}} \right) + \frac{1}{2} \cdot \frac{V_i}{N} \cdot d \cdot T_s \tag{7}$$

where α is the ratio of R_{mc} to R_{mo} ($\alpha = R_{\text{mc}}/R_{\text{mo}}$). Similarly, the peak flux in the central leg when the duty ratio is less or greater than 0.5 is, respectively, given by

$$\begin{cases} \Phi_{\text{cp\_d}\le 0.5} = \Phi_c + \dfrac{1}{2}\Phi_{\text{cpp\_d}\le 0.5} = \dfrac{2 \cdot N \cdot I_{\text{Lave}}}{R_{\text{mo}} \cdot (1+2\alpha)} + \dfrac{1}{2} \cdot \dfrac{1-2d}{1-d} \cdot \dfrac{V_i}{N} \cdot d \cdot T_s \\ \Phi_{\text{cp\_d}>0.5} = \Phi_c + \dfrac{1}{2}\Phi_{\text{cpp\_d}>0.5} = \dfrac{2 \cdot N \cdot I_{\text{Lave}}}{R_{\text{mo}} \cdot (1+2\alpha)} + \dfrac{1}{2} \cdot \dfrac{2d-1}{d} \cdot \dfrac{V_i}{N} \cdot d \cdot T_s. \end{cases} \tag{8}$$

Based on the magnetic circuit model shown in Fig. 5, the mutual inductance M and the leakage inductance L_{lk} are described

as follows:

$$\begin{cases} M = N^2 \cdot \dfrac{R_{\rm mc}}{R_{\rm mo}^2 + 2 \cdot R_{\rm mo} \cdot R_{\rm mc}} \\ L_{\rm lk} = N^2 \cdot \dfrac{1}{R_{\rm mo} + 2 \cdot R_{\rm mc}}. \end{cases} \tag{9}$$

Therefore, the relationship between the coupling coefficient k and the ratio of magnetic reluctance α is as follows:

$$k = \frac{M}{L_{\rm self}} = \frac{M}{M + L_{\rm lk}} = \frac{\alpha}{1+\alpha}, \quad \alpha = \frac{k}{1-k}. \tag{10}$$

From (10), it can be deduced that the coupling coefficient k is related to the ratio of magnetic reluctance only. In addition, by solving (4), (9), and (10) together, the dc flux related to the unbalanced current, $\Phi_{\rm o\_\delta}$ can be expressed as follows:

$$\begin{aligned} \Phi_{\rm o\_\delta} &= N \cdot I_{\rm Lave} \cdot \frac{\delta}{R_{\rm mo}} = N \cdot I_{\rm Lave} \cdot \delta \cdot (L_{\rm lk} + 2M) \\ &= N \cdot I_{\rm Lave} \cdot \delta \cdot L_{\rm self} \cdot (1 \ + \ k). \end{aligned} \tag{11}$$

Based on (11), it can be concluded that in the case of high coupling factor k, the influence of a small current unbalance (i.e., small value of δ) on the dc flux will be significantly high in the LCI configuration [26], [27]. Therefore, it is important to insert a small air gap into the outer legs to improve the immunity to the unbalanced currents, and to minimize the effect of dc-biased magnetization by adjusting the value of the coupling factor k.

B. Inductor Ripple Current Analysis

Inductor ripple current is an important factor in designing magnetic devices. Because the ripple current flows in the inductor windings, it influences the maximum current ratings of the power devices, the power conversion efficiency, and the load range that can be operated in the continuous current mode (CCM). In this paper, CCM is assumed because the interleaved multiphase boost converter is often applied in high-power applications, and inductors are usually designed at the maximum power rating in the converter.

In CCM operation ranges, the inductor ripple current is expressed by the following equation, regardless of whether the current is balanced or unbalanced

$$\begin{cases} I_{\rm Lpp\_d\le 0.5} = R_{\rm mo} \left(1 + \alpha \cdot \dfrac{1-2\cdot d}{1-d}\right) \cdot \dfrac{V_i}{N^2} \cdot d \cdot T_s \\ I_{\rm Lpp\_d>0.5} = R_{\rm mo} \left(1 + \alpha \cdot \dfrac{2\cdot d-1}{d}\right) \cdot \dfrac{V_i}{N^2} \cdot d \cdot T_s. \end{cases} \tag{12}$$

C. Peak Flux Normalized by the Inductor Ripple Current

Based on (7), (8), and (12), it is clear that the magnetic circuit parameters $R_{\rm mo}$, $R_{\rm mc}$, and N, influence both the peak flux and the inductor ripple current. Therefore, to evaluate the downsizing effect of the LCI under the dc-biased magnetization condition, the maximum fluxes in the outer and the center legs shall be derived as a function of the inductor ripple current.

The peak fluxes in the outer leg within the ranges of the duty ratio $d \le 0.5$, $d > 0.5$ are given by the following equations, which are obtained by substituting (12) into (7) to eliminate $R_{\rm mo}$

$$\begin{cases} \Phi_{\rm op\_d\le 0.5} = \dfrac{V_i}{N} \cdot \left(\dfrac{\delta \cdot (1+2\cdot\alpha)+1}{1+2\cdot\alpha} \cdot \left(1+\alpha \cdot \dfrac{1-2\cdot d}{1-d}\right) \cdot \dfrac{I_{\rm Lave}}{I_{\rm Lpp}} + \dfrac{1}{2} \right) \cdot d \cdot T_s \\ \Phi_{\rm op\_d>0.5} = \dfrac{V_i}{N} \cdot \left(\dfrac{\delta \cdot (1+2\cdot\alpha)+1}{1+2\cdot\alpha} \cdot \left(1+\alpha \cdot \dfrac{2\cdot d-1}{d}\right) \cdot \dfrac{I_{\rm Lave}}{I_{\rm Lpp}} + \dfrac{1}{2} \right) \cdot d \cdot T_s \end{cases} \tag{13}$$

In the same way, the peak fluxes in the central leg are given by

$$\begin{cases} \Phi_{\rm cp\_d\le 0.5} = \dfrac{V_i}{N} \cdot \left(\dfrac{2}{1+2\cdot\alpha} \cdot \left(1+\alpha \cdot \dfrac{1-2\cdot d}{1-d}\right) \cdot \dfrac{I_{\rm Lave}}{I_{\rm Lpp}} + \dfrac{1}{2} \cdot \dfrac{1-2\cdot d}{1-d} \right) \cdot d \cdot T_s \\ \Phi_{\rm cp\_d>0.5} = \dfrac{V_i}{N} \cdot \left(\dfrac{2}{1+2\cdot\alpha} \cdot \left(1+\alpha \cdot \dfrac{2\cdot d-1}{d}\right) \cdot \dfrac{I_{\rm Lave}}{I_{\rm Lpp}} + \dfrac{1}{2} \cdot \dfrac{2\cdot d-1}{d} \right) \cdot d \cdot T_s \end{cases}. \tag{14}$$

On the other hand, in the case of the noncoupled inductor, the peak flux can be expressed as a function of the current unbalance as follows:

$$\Phi_{\rm np} = \frac{V_i}{N} \cdot \left\{ \frac{I_{\rm Lave}}{I_{\rm Lpp}} \cdot (\delta + 1) + \frac{1}{2} \right\} \cdot d \cdot T_s. \tag{15}$$

Equation (15) is derived to help investigate the reduction of the magnetic core volume of the LCI compared with that of the noncoupled inductor.

D. Comparisons of Peak Fluxes and Core Volume

Equations (13)–(15) describe the peak fluxes in the outer leg, the central leg of the LCI, and the noncoupled inductor, respectively. These equations will help us to evaluate the core volume in each case for dc-biased magnetization. In addition, this evaluation is helpful in selecting a suitable magnetic core, since it provides information about which leg has the higher flux density in the LCI configuration. The evaluation items to compare each peak flux, $\Phi_{\rm cp}\,(\delta = 0 - 0.02)/\Phi_{\rm op}\,(\delta = 0 - 0.02)$, $\Phi_{\rm op}\,(\delta = 0.01 - 0.03)/\Phi_{\rm op}\,(\delta = 0)$, and $\Phi_{\rm op}\,(\delta = 0 - 0.02)/\Phi_{\rm np}\,(\delta = 0 - 0.02)$ are, respectively compared to confirm the influence of dc-biased magnetization. These comparison results are also useful in describing the relationship between the section area of the central and the outer legs to obtain a uniform and constant value of flux density in the magnetic core. All comparisons are carried out under the condition that the ratio of the ripple current to the average current $I_{\rm Lpp}/I_{\rm Lave}$ is 0.3.

First, using (13) and (14), the ratio of $\Phi_{\rm cp}\,(\delta = 0 - 0.02)$ to $\Phi_{\rm op}\,(\delta = 0 - 0.02)$ is obtained, as shown in Fig. 6(a)–(c). As a comparison condition, δ is varied from 0 to 0.02. As can be seen in Fig. 6(a)–(c), the peak flux $\Phi_{\rm cp}$ in the central leg is always less

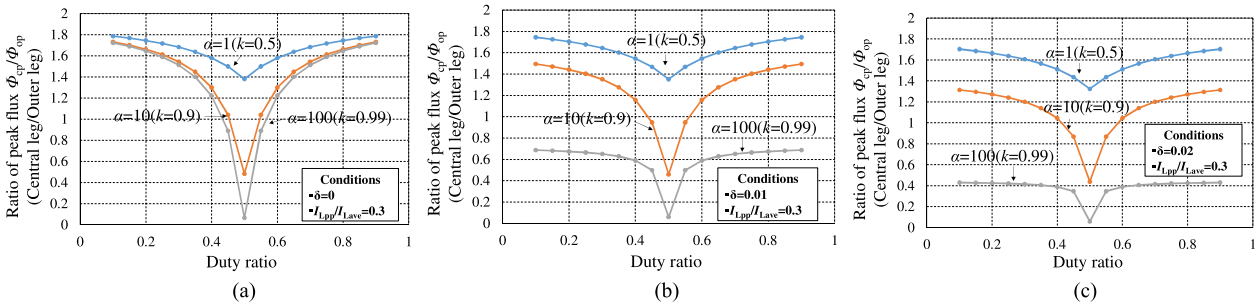

Fig. 6. Ratio of the peak flux in the central leg to that in the outer leg. (a) $\delta = 0$. (b) $\delta = 0.01$. (c) $\delta = 0.02$.

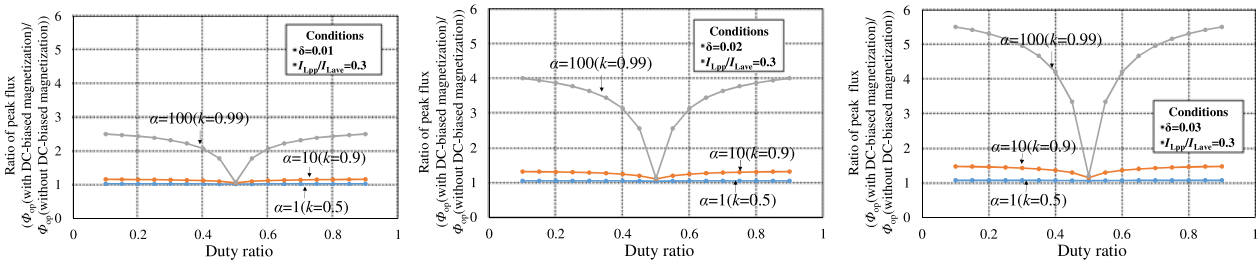

Fig. 7. Ratio of the peak flux in the outer leg with DC-biased magnetization to that in the outer leg without DC-biased magnetization. (a) $\delta = 0.01$. (b) $\delta = 0.02$. (c) $\delta = 0.03$.

than twice its value in the outer leg in all ranges of the duty ratio and under any δ conditions. Usually, magnetic cores with the EE or EI shape have twice the sectional area in the central leg as compared with the outer legs. In this context, if the sectional area in the central leg is larger than twice its value in the outer leg, the flux density in the outer leg is always the highest in the core. In addition, when unbalanced current flows into the winding of the LCI with a high coupling coefficient, the peak flux $\Phi_{\rm op}$ in the outer leg increases significantly in comparison with $\Phi_{\rm cp}$ in the central leg, because a higher coupling coefficient k means lower magnetic reluctance $R_{\rm mo}$, which helps to generate a larger dc flux in the outer leg under unbalanced current conditions.

Second, Fig. 7(a)–(c) shows the ratio of the peak flux $\Phi_{\rm op}$ with dc-biased magnetization ($\delta = 0.01$–0.03) to $\Phi_{\rm op}$ without dc-biased magnetization ($\delta = 0$). This comparison is conducted to investigate the influence of the unbalanced current factor δ under the same coupling coefficient condition. As shown in Fig. 7(a)–(c), if the LCI is designed with a higher k (i.e., $k = 0.99$) and unbalanced current occurs between each phase, it leads to an increase of the peak flux $\Phi_{\rm op}$ in the outer leg under unbalanced conditions and, consequently, magnetic saturation may occur if the LCI is designed assuming balanced current conditions. When magnetic saturation occurs, the inductance values of the LCI drop dramatically and the inductor current ripple increases considerably, causing conduction losses (in both of the inductor winding and power devices) to increase. In the worst case, the converter may be stopped by the overcurrent protection mechanism. As previously mentioned, the vertical axis shown in Fig. 7(a)–(c) means that the ratio of peak flux with dc-biased magnetization to that without dc-biased magnetization. In other words, the vertical axis also means the ratio of the sectional area in the outer leg designed to handle the same flux density under the balanced and unbalanced conditions, respectively, as understood from (2). Therefore, the outbreak of the unbalanced current is related to a reduction in the downsizing effect of LCI. On the other hand, within lower values of the coupling coefficient (i.e., $k = 0.5$), the ratio of the peak flux under unbalanced $\Phi_{\rm op}$ ($\delta = 0.01 - 0.03$) to that under balanced $\Phi_{\rm op}$ ($\delta = 0$) is considerably small. This is also consistent with (11). However, a lower coupling coefficient considerably reduces the downsizing effect of LCI as compared with noncoupled inductors as follows.

Finally, using (13) and (15), peak flux $\Phi_{\rm op}$ ($\delta = 0 - 0.02$) in the outer leg is compared with $\Phi_{\rm np}$ ($\delta = 0 - 0.02$) in the noncoupled inductor. In this comparison, both the coupled and the noncoupled inductors have the same number of turns because the number of turns also affects the values of their peak fluxes. The purpose of this investigation is to confirm the reduction in the downsizing effect of LCI in comparison with a noncoupled inductor when k and δ are varied. Fig. 8(a)–(c) show the ratio of $\Phi_{\rm op}$ to $\Phi_{\rm np}$ under the same δ conditions. The vertical axis in this figure also means that the ratio of sectional area $A_{\rm o}$ in the outer leg to $A_{\rm non}$ of the noncoupled inductor is designed to have the same flux density. As can be seen in Fig. 8(a)–(c), if LCI with a higher k is used under the $\delta = 0$ condition, greater reduction in $\Phi_{\rm op}$ can be obtained as compared with that of a noncoupled inductor. Therefore, the downsizing of the sectional area A_o in the outer leg of LCI can be realized as compared with that of a noncoupled inductor. This means that a higher coupling coefficient helps to reduce the overall core volume of LCI under the current balancing condition $\delta = 0$. On the other hand, when higher unbalanced currents flow into the windings of LCI with higher k, $\Phi_{\rm op}$ greatly increases compared with $\Phi_{\rm np}$. Therefore, a higher k is not always suitable for downsizing of magnetic core under unbalanced average current condition. As shown in Figs. (6)–(8), the coupling coefficient value of 0.99

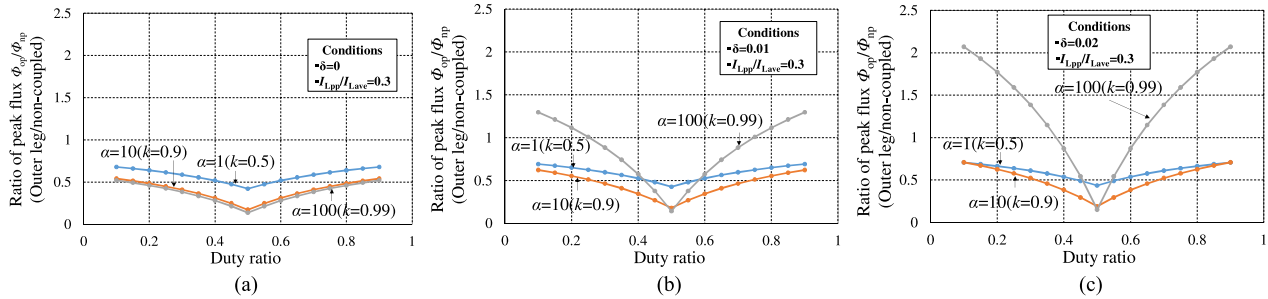

Fig. 8. Ratio of the peak flux in the outer leg to that in the noncoupled inductor. (a) $\delta = 0$. (b) $\delta = 0.01$. (c) $\delta = 0.02$.

is given as an extreme example to investigate the influence on dc-biased magnetization. However, a high coupling coefficient such as 0.99 or a value close to it could be obtained by using high-permeability magnetic materials such as nanocrystalline, amorphous cores, or electrical steel sheets.

Then, to clarify the effect of dc-biased magnetization on the core volume of LCI, a calculation method of core volume based on the area product method [27], [35] is introduced. The calculation of core volume is carried out by estimation. The definitions of the core size for the estimated core are shown in Fig. 9. The shape of the sectional area $A_{\rm o}$ in the outer leg of LCI, $A_{\rm non}$ of the noncoupled inductor, and the winding area $A_{\rm w}$ to wind the windings to the core, are defined as square for analytical convenience. In this structure, the core volume of LCI, $\mathrm{Vol}_{\rm coupled}$ can be calculated as follows:

$$\begin{aligned}\mathrm{Vol}_{\rm coupled} =& \underbrace{\left\{\left(\sqrt{A_o}+\sqrt{A_w}\right)\cdot\left(2\sqrt{A_o}+\sqrt{A_w}\right)\cdot\sqrt{A_o}-A_w\cdot\sqrt{A_o}\right\}}_{\text{Core volume in outer leg}}\cdot 2\\ &+\underbrace{\left(2\sqrt{A_o}+\sqrt{A_w}\right)\cdot\frac{A_c}{\sqrt{A_o}}\cdot\sqrt{A_o}}_{\text{Core volume in central leg}}\\ &=2\cdot\sqrt{A_o}\cdot(A_c+2A_o)+(A_c+6A_o)\cdot\sqrt{A_w}.\end{aligned} \tag{16}$$

Then, $A_{\rm o}$ and $A_{\rm c}$ described in (16) can be converted as follows:

$$\begin{cases} A_o = \dfrac{\Phi_{\rm op}}{B_{\max}} = \dfrac{\Phi_{\rm np}}{B_{\max}}\cdot\dfrac{\Phi_{\rm op}}{\Phi_{\rm np}} = A_{\rm non}\cdot\dfrac{\Phi_{\rm op}}{\Phi_{\rm np}} \\ A_c = \dfrac{\Phi_{\rm cp}}{B_{\max}} = \dfrac{\Phi_{\rm np}}{B_{\max}}\cdot\dfrac{\Phi_{\rm op}}{\Phi_{\rm np}}\cdot\dfrac{\Phi_{\rm cp}}{\Phi_{\rm op}} = A_{\rm non}\cdot\dfrac{\Phi_{\rm op}}{\Phi_{\rm np}}\cdot\dfrac{\Phi_{\rm cp}}{\Phi_{\rm op}}. \end{cases} \tag{17}$$

Likewise, the total core volume of the noncoupled inductors, $\mathrm{Vol}_{\rm total\_non}$ can be calculated as follows:

$$\begin{aligned}\mathrm{Vol}_{\rm total\_non} =& \underbrace{\left\{\left(2\sqrt{A_{\rm non}}+\sqrt{A_w}\right)^2\cdot\sqrt{A_{\rm non}}-A_w\cdot\sqrt{A_{\rm non}}\right\}}_{\text{core volume per a phase}}\cdot 2\\ &=8\cdot A_{\rm non}\cdot\left(\sqrt{A_{\rm non}}+\sqrt{A_w}\right).\end{aligned} \tag{18}$$

Therefore, the ratio of $\mathrm{Vol}_{\rm coupled}$ to $\mathrm{Vol}_{\rm total\_non}$ is given by the following equation:

$$\begin{aligned}&\frac{\mathrm{Vol}_{\rm coupled}}{\mathrm{Vol}_{\rm total\_non}}\\ &=\frac{\frac{\Phi_{\rm op}}{\Phi_{\rm np}}\left(\sqrt{A_w}\cdot\left(6+\frac{\Phi_{\rm cp}}{\Phi_{\rm op}}\right)+2\left(2+\frac{\Phi_{\rm cp}}{\Phi_{\rm op}}\right)\cdot\sqrt{A_{\rm non}\cdot\frac{\Phi_{\rm op}}{\Phi_{\rm np}}}\right)}{8\cdot\left(\sqrt{A_{\rm non}}+\sqrt{A_w}\right)}.\end{aligned} \tag{19}$$

Therefore, the estimated core volume of LCI and that of noncoupled inductors can be compared by utilizing (13)–(15) and (19). The ratio of $\mathrm{Vol}_{\rm coupled}$ to $\mathrm{Vol}_{\rm total\_non}$ is shown in Fig. 10. The preconditions to illustrate Fig. 10 are also shown in the same figure. As can be seen in this figure, $\mathrm{Vol}_{\rm coupled}$ can be significantly reduced at higher coupling coefficients when $\delta = 0$. However, with increasing δ, higher k degrades the downsizing effect of LCI. We summarize as follows.

1) Under balanced current condition: LCI with a high coupling coefficient is effective to downsize the core volume. As the peak flux in the outer leg can be reduced, the sectional area of the outer leg can be downsized.
2) Under unbalanced current conditions: LCI with a high coupling coefficient leads to an increase in the volume of the magnetic core to avoid magnetic saturation.

It can be concluded that there is a tradeoff between handling the dc-biased magnetization and downsizing the magnetic components. This tradeoff is directly related to the coupling coefficient of the LCI. Therefore, selecting the optimum value of the coupling factor is important to obtain immunity to the phase unbalanced currents and downsizing the magnetic core volume.

IV. Magnetic Design Method for Coupled Inductor

A. Determining Optimal Coupling Coefficient

The purpose of the proposed design method is to obtain optimal magnetic circuit parameters such as $R_{\rm mo}$, $R_{\rm mc}$, and N under any unbalanced condition. In order to downsize the magnetic core of the LCI compared with noncoupled inductors, the optimal coupling coefficient k considering any unbalanced current factor δ shall be derived. Furthermore, the core volume of the outer legs of the LCI occupy a large proportion of the total volume of LCI as can be seen in Fig. 9, because the central leg is a part of the core. Therefore, the condition that the ratio of peak flux $\Phi_{\rm op}$ to $\Phi_{\rm np}$ becomes the lowest value is one of the optimal

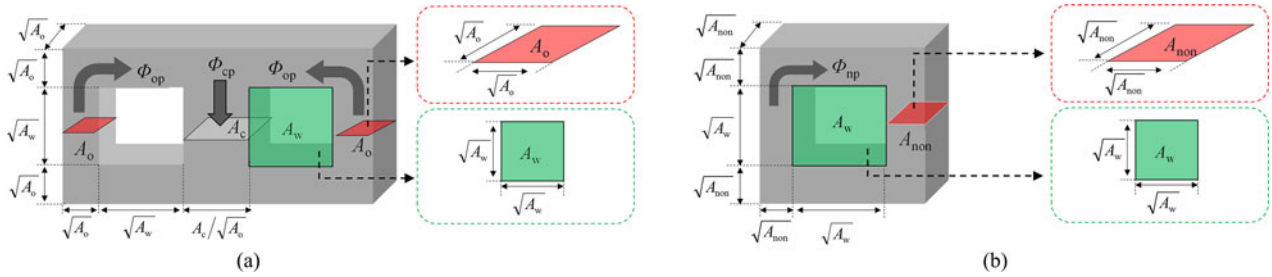

Fig. 9. Definitions of the estimated core. (a) Coupled inductor. (b) Noncoupled inductor for per a phase.

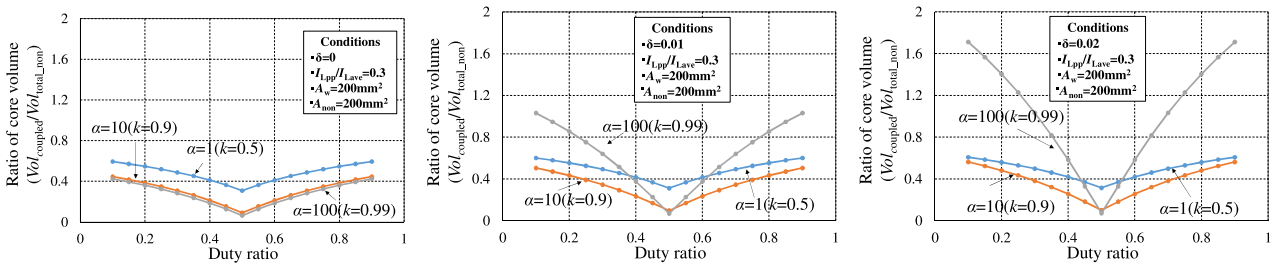

Fig. 10. Ratio of the core volume of LCI to that of noncoupled inductors. (a) $\delta = 0$. (b) $\delta = 0.01$. (c) $\delta = 0.02$.

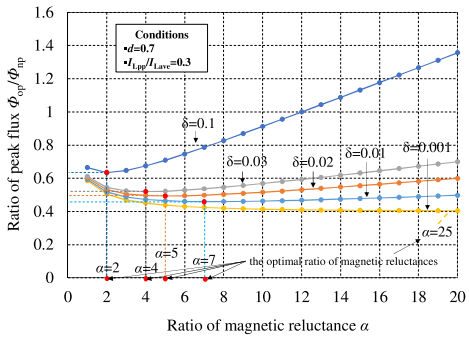

Fig. 11. Relationship between ratio of peak flux $(\Phi_{\rm op}/\Phi_{\rm np})$ and ratio of magnetic reluctance α.

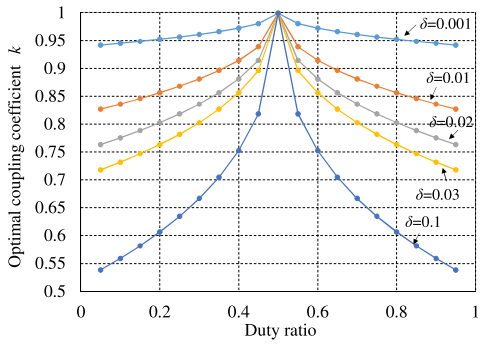

Fig. 12. Optimal coupling coefficient considering DC-biased magnetization.

design points to downsize the core volume of LCI. To identify an optimal α (or an optimal k), Fig. 11 shows the ratio of $\Phi_{\rm op}$ to $\Phi_{\rm np}$ when $\delta = 0.001$–0.1 and d is fixed at 0.7. As shown in Fig. 11, there is one optimal value of α where $\Phi_{\rm op}/\Phi_{\rm np}$ is minimum. To identify the optimal α, the following equations have to be satisfied:

$$\begin{cases} \dfrac{d\left(\Phi_{\rm op\_d\le 0.5}/\Phi_{\rm np}\right)}{d\alpha} = 0 \\ \dfrac{d\left(\Phi_{\rm op\_d>0.5}/\Phi_{\rm np}\right)}{d\alpha} = 0. \end{cases} \tag{20}$$

By solving (20), the optimal α can be obtained within the ranges of duty ratio less or greater than 0.5, respectively

$$\begin{cases} \alpha_{\rm d\le 0.5} = \dfrac{\delta(1-2d) \pm \sqrt{\delta(1-2d)}}{2\delta(2d-1)} \\ \alpha_{\rm d>0.5} = \dfrac{\delta(2d-1) \pm \sqrt{\delta(2d-1)}}{2\delta(1-2d)}. \end{cases} \tag{21}$$

Although there are two solutions in (21) within the ranges of $d \le 0.5$, $d > 0.5$, when the second term in (21) is positive, α is not effective because it always becomes negative. This value cannot be used in practical design. Therefore, the effective value of α can be obtained as follows:

$$\begin{cases} \alpha_{\rm d\le 0.5} = \dfrac{\delta(1-2d) - \sqrt{\delta(1-2d)}}{2\delta(2d-1)} \\ \alpha_{\rm d>0.5} = \dfrac{\delta(2d-1) - \sqrt{\delta(2d-1)}}{2\delta(1-2d)}. \end{cases} \tag{22}$$

As shown in (22), the optimal α depends on only the duty ratio and the maximum permissible factor δ. Using (10) and (22), the relationship between the optimal k and duty ratio d under any δ condition is shown in Fig. 12. As shown in Fig. 12, the coupling coefficient considering a maximum permissible factor δ is relatively high at $d = 0.5$. However, a lower coupling coefficient is needed at extreme duty ratios such as $d = 0.1$ and 0.9 or with increasing unbalanced current factor δ, as a feature of the optimal k. Figs. 13 and 14, respectively, show the ratio of $\Phi_{\rm op}$ $(\delta = 0.001 - 0.1)/\Phi_{\rm np}$ $(\delta = 0.001 - 0.1)$ and the

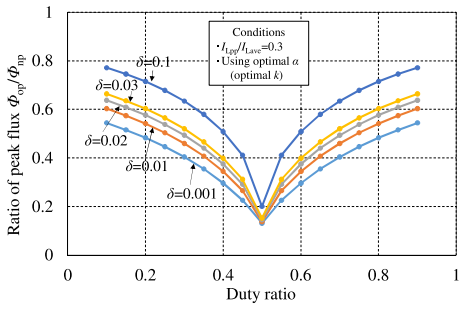

Fig. 13. Ratio of peak flux $(\Phi_{\rm op}/\Phi_{\rm np})$ using the optimal α under DC-biased magnetization condition.

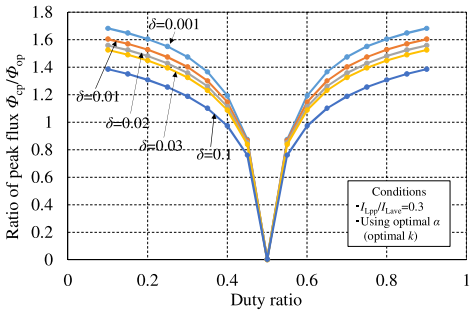

Fig. 14. Ratio of peak magnetic fluxes $(\Phi_{\rm cp}/\Phi_{\rm op})$ using the optimal α under DC-biased magnetization condition.

ratio of $\Phi_{\rm cp}$ $(\delta = 0.001 - 0.1)/\Phi_{\rm op}$ $(\delta = 0.001 - 0.1)$ when the optimal α derived from (22) is used. It can be seen that as the operating duty ratio d approaches the duty ratio limits (for instance 0.1 or 0.9), the downsizing effect of the sectional area $A_{\rm o}$ in the outer leg becomes smaller compared with that of the noncoupled inductor. Therefore, when the two-phase interleaved boost converter with LCI is employed in renewable energy systems that require a high voltage gain [10], the downsizing effect is relatively low. On the other hand, as shown in Fig. 14, the ratio of peak flux $(\Phi_{\rm cp}/\Phi_{\rm op})$ reduces with increasing δ. This is because the unbalanced current factor δ only affect the increase of $\Phi_{\rm op}$, and $\Phi_{\rm cp}/\Phi_{\rm op}$ becomes smaller with increasing δ.Although the total core volume of LCI is mainly occupied by the outer legs, the core volume of the central leg also impacts the total volume of LCI. Therefore, to demonstrate the effectiveness of the optimal k, the core volume of LCI and that of the noncoupled inductor are compared when the coupling coefficient k is 0.1–0.99. In addition, since the optimal k is affected by not only d but also δ, comparative studies on the two conditions are conducted to investigate the impact of not considering the peak flux in the central leg: One is assumed on the condition that δ is fixed as 0.03, and d is varied from 0.1 to 0.9. The other is assumed on the condition that d is fixed as 0.7, and δ is varied from 0.001 to 0.1. By substituting (10) into (13) and (14), and then calculating (19), the ratio of the core volume of LCI to that of noncoupled inductors can be obtained. The comparison results of the core volumes of LCI and the noncoupled inductor are shown in Fig. 15(a) and (b), respectively. As can be seen in Fig. 15(a) and (b), there is a slight error between the coupling coefficient that results in the maximum downsizing effect and

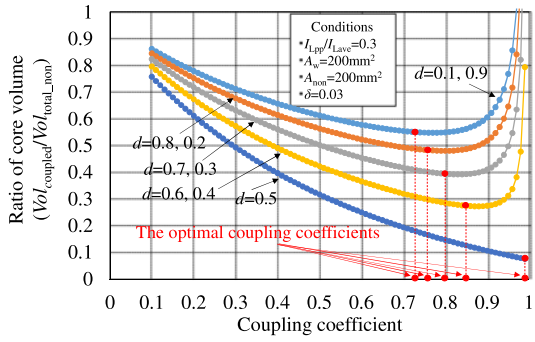

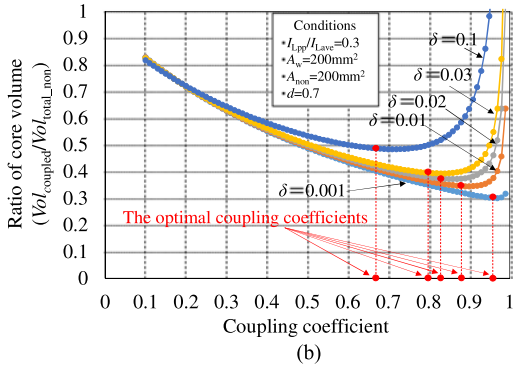

Fig. 15. Ratio of core volume of LCI to that of a noncoupled inductor when k is varied. (a) Condition of δ is fixed as 0.03. (b) d is fixed as 0.7.

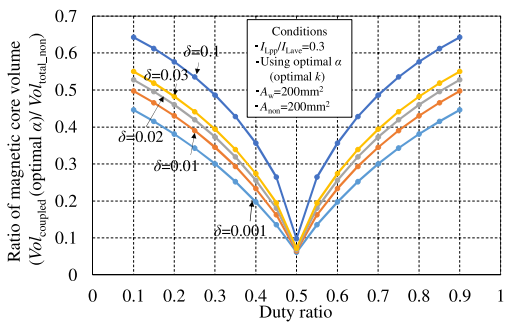

Fig. 16. Downsizing effect of core size with optimal coupling coefficient.

the optimal k plotted in red points in these figures. However, the optimal k can be identified as the design point with a high downsizing effect. Therefore, the effectiveness of the optimal k is proved. Finally, the downsizing effect of LCI with the optimal k is calculated. Fig. 16 shows the ratio of core volume of LCI with the optimal k to that of noncoupled inductors. As can be seen in Fig. 16, LCI designed by the optimal k can significantly downsize the core volume while compensating dc-biased magnetization. Even if $\delta = 0.1$ and $d = 0.1$–0.9, LCI can be downsized by at least 30% as compared with the total volume of noncoupled inductors.

B. *Proposed Magnetic Design Method*

In this section, the magnetic design method for LCI is proposed on the basis of the analysis results. In addition, the effectiveness of LCI designed by the proposed design method is

TABLE I
CIRCUIT PARAMETERS

Input voltage	$V_{\rm i}$	50V
Output voltage	$V_{\rm o}$	120 V
Input power	$P_{\rm i}$	1 kW
Duty ratio	d	0.583
Switching frequency	$f_{\rm s}$	50 kHz
Inductor average current	$I_{\rm Lave}$	10 A
Maximum permissible percentage of unbalanced inductor average currents	δ	0.05
Inductor ripple current	$I_{\rm Lpp}$	3 A
Ratio of ripple current	$I_{\rm Lpp}/I_{\rm Lave}$	0.3
Maximum flux density	$B_{\rm max}$	250 mT
Maximum flux	$\Phi_{\rm max}$	46 μWb

TABLE II
MAGNETIC MATERIAL PROPERTY AND CORE SIZE

Core size		EC70 (TDK)
Core material		Ferrites (PC40)
Relative permeability	$\mu_{\rm r}$	2300
Saturation flux density	$B_{\rm sat\,(100\,^\circ C)}$	380 mT
Residual magnetic flux density	$B_{\rm r}$	125 mT
Sectional area in outer leg	$A_{\rm o}$	184 mm^2
Sectional area in central leg	$A_{\rm c}$	211 mm^2
Effective magnetic path length	$l_{\rm e}$	144 mm

confirmed through this evaluation. The circuit parameters and the magnetic parameters for this evaluation are shown in Tables I and II. The duty ratio of the boost converter is chosen to be 0.583 as a practical value, since the boost converter in a well-known hybrid electric vehicle, Toyota PRIUS (2nd version), uses this value [36]. The generic magnetic core (material: ferrite (PC40), size: EC70) is selected for the magnetic core of LCI [37]. This core can be obtained easily with no need to custom-build special cores. In this design, the maximum permissible percentage of unbalanced inductor average currents, δ is assumed within 5%, considering offset voltages, nonlinearity, and temperature dependability of hall-effect current sensors. The gain error of the hall-effect current sensors has to be considered as several percent of the gain error in practical design [38]. In addition, the relationship between the unbalanced current and gain error of the current sensor is shown in Appendix II. The design flowchart of the novel design method is shown in Fig. 17. The contents in each step in the process of the proposed design method are given below:

Step 1: The optimal α and coupling coefficient k are derived. Using (22) in the range of $d > 0.5$ and (10), α and k are obtained as 4.98 and 0.83, respectively.

Step 2: The number of turns in each phase is decided to fulfill the design parameters. As mentioned in Section III-D, there are two peak fluxes in the outer leg and the central leg in the core. Therefore, it is required to investigate which leg in LCI has higher flux density by using the following relation:

$$\frac{B_{\rm op}}{B_{\rm cp}} = \frac{\Phi_o/A_o}{\Phi_c/A_c} \tag{23}$$

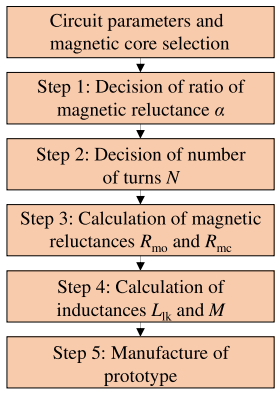

Fig. 17. Design flowchart of the novel design method considering DC-biased magnetization, caused by little unbalanced currents.

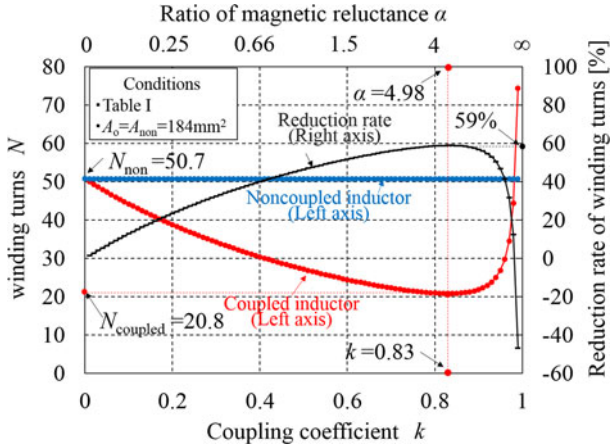

Fig. 18. Change trend of the number of turns of the coupled and noncoupled inductors when α is varied.

where $B_{\rm op}$ and $B_{\rm cp}$ are the peak fluxes in the outer leg and the central leg, respectively. By substituting (13) and (14) into (23), $B_{\rm op}/B_{\rm cp}$ is calculated as 1.16. Therefore, the flux density should be regulated at the outer leg. Considering (2) and (13), which comply with the condition of $\Phi_{\rm op} \le \Phi_{\rm max}$, the following equation can be obtained:

$$N_{\rm d>0.5} \ge \frac{\left\{I_{\rm Lave}\cdot\left(1+\alpha\cdot\frac{2d-1}{d}\right)\cdot\left(\delta+\frac{1}{1+2\alpha}\right)+\frac{1}{2}\cdot I_{\rm Lpp}\right\}\cdot V_i\cdot d\cdot T_s}{I_{\rm Lpp}\cdot B_{\rm max}\cdot A_o}. \tag{24}$$

In this case, the effective range of the number of turns is calculated as $N \ge 20.81$; therefore, N is chosen as 21 turns.

Then, to validate the effectiveness of the optimal α derived in Step 1, the number of turns of LCI are compared with that of noncoupled inductors when α is varied. Fig. 18 shows the change trend of the number of turns of LCI and that of the noncoupled inductor. The coupling factor k and the reluctance ratio α are simultaneously shown on the horizontal axis, according to (10). It is clear that there is an optimum value of the coupling factor where the number of turns can be minimized in the LCI configuration. In addition, this optimal coupling coefficient can

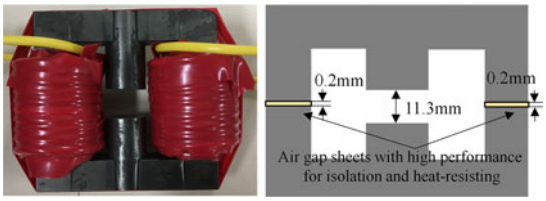

Fig. 19. Prototype of the coupled inductor with air gap in the outer legs (proposed design method).

be derived in Step 1. Other than the optimum value point on the curve, we have the following two conditions:

1) when the coupling factor is higher than the optimum value: the number of turns increases due to the influence of the dc-biased magnetization, as mentioned earlier in (11);
2) when the coupling factor is lower than the optimum value: in this case, the number of turns increases as the LCI characteristic becomes similar to the noncoupled inductor (i.e., low value of the coupling factor makes the LCI act as two independent magnetic cores).

In the aforementioned two conditions, the winding volume and conduction losses are expected to increase. On the other hand, the number of turns of the noncoupled inductor is calculated as 50.7 turns on the basis of (15). This value is constant because the coupling coefficient has no influence. Consequently, a reduction of 59% in the number of turns can be achieved at the optimum value of the coupling factor $(k = 0.83)$.

Step 3: The magnetic reluctances $R_{\rm mo}$ and $R_{\rm mc}$ in the outer legs and the central leg, respectively, are calculated. The magnetic reluctance $R_{\rm mo}$ in the outer leg can be calculated from (12) because *N*, α, and the other parameters in (12) have already been decided. In this case, $R_{\rm mo}$ is calculated as $R_{\rm mo} = 0.93$ A/μWb, and $R_{\rm mc}$ is also calculated as 4.66 A/μWb from $\alpha = R_{\rm mc}/R_{\rm mo}$.

Step 4: Design values of each inductance have to be derived by using (9) because the magnetic reluctances cannot be measured directly. As the design value, the leakage inductance $L_{\rm lk}$ is 43 μH, and the mutual inductance *M* is calculated as 213 μH.

Step 5: The final step is to build the prototype. Usually, the values of the magnetic reluctances $R_{\rm mo}$ and $R_{\rm mc}$ in the prototype are estimated by measuring inductance values $L_{\rm lk}$ and *M* because these values cannot be measured directly. This is because the magnetic reluctance value calculated from the geometrical structure has errors caused by the tiny air gaps at the junction of the core, the fringing flux at air gap, and the uneven flow of the magnetic flux in the core. To estimate $R_{\rm mo}$ values in the prototype, the following relationship is used

$$R_{\rm mo} = \frac{N^2}{L_{\rm lk} + 2M}. \tag{25}$$

Equation (25) is derived from (9). By using this relationship, the air gap length of the outer legs is varied by inserting a thin film that has excellent isolation and heat-resisting properties. The value of $R_{\rm mo}$ can be adjusted to the designed value. As a result, the air gap length in the outer leg is fixed at 0.2 mm.

TABLE III
MAGNETIC PARAMTERS (PROPOSED DESIGN)

Winding turn number	N	21
Magnetic reluctance of the outer leg (designed value)	R^*_{mo}	0.93 A/μWb
Magnetic reluctance of the central leg (the converted value from measured inductance value)	$R_{\rm mo}$	0.91 A/μWb
Magnetic reluctance of the central leg (designed value)	$R^*_{\rm mc}$	4.66 A/μWb
Magnetic reluctance of the central leg (the converted value from measured inductance value)	$R_{\rm mc}$	4.67 A/μWb

TABLE IV
INDUCTANCE VALUES (PROPOSED DESIGN)

Mutual inductance (designed value)	M^*	213 μH
Mutual inductance (measured value)	M	220 μH
Leakage inductance (designed value)	$L_{\rm lk}{}^*$	43 μH
Leakage inductance (measured value of phase 1)	$L_{\rm lk1}$	43 μH
Leakage inductance (measured value of phase 2)	$L_{\rm lk2}$	43 μH
Coupling coefficient (designed value)	k^*	0.83
Coupling coefficient (measured value)	k	0.83

TABLE V
MAGNETIC PARAMETERS (CONVENTIONAL DESIGN)

Winding turn number	N	14
Magnetic reluctance of the outer leg (designed value)	$R_{\rm mo}{}^*$	0.18 A/μWb
Magnetic reluctance of the central leg (the converted value from measured inductance value)	$R_{\rm mo}$	0.18 A/μWb
Magnetic reluctance of the central leg (designed value)	$R_{\rm mc}{}^*$	2.89 A/μWb
Magnetic reluctance of the central leg (the converted value from measured inductance value)	$R_{\rm mc}$	2.88 A/μWb

Then, to adjust the magnetic reluctance $R_{\rm mc}$ in the central leg, the central leg is cut to obtain the designed reluctance value. The air gap length in the central leg is set to 11.3 mm. The prototype of the LCI is shown in Fig. 19. In addition, the designed magnetic parameters and converted magnetic reluctance values from the measured inductances are summarized in Table III. The designed and measured inductance values are also shown in Table IV. There is only a slight error between the designed and measured values, as shown in Tables III and IV. Therefore, the appropriateness of the implementation method is confirmed. Furthermore, to verify the effectiveness of the proposed design method with the optimal *k* from the perspective of reliability, a prototype based on the conventional design method given in [27] is made. The feature of the conventional design method is that there is no air gap in the outer legs. The advantage of this is that the downsizing effect is higher than the proposed design method. However, if unbalanced currents flow into the windings of the LCI designed by the conventional design method, magnetic saturation can easily occur because the dc-biased magnetization is not considered, and the designed coupling coefficient value is comparatively high. Similarly, the magnetic circuit parameters of LCI based on the conventional design method are shown in Tables V and VI. The conventional LCI is shown in Fig. 20.

TABLE VI
INDUCTANCE VALUES (CONVENTIONAL DESIGN)

Mutual inductance (designed value)	M^*	523 μH
Mutual inductance (measured value)	M	522 μH
Leakage inductance (designed value)	$L_{\mathrm{lk}}{}^*$	34 μH
Leakage inductance (measured value of phase 1)	$L_{\mathrm{lk}1}$	33 μH
Leakage inductance (measured value of phase 2)	$L_{\mathrm{lk}2}$	33 μH
Coupling coefficient (designed value)	k^*	0.94
Coupling coefficient (measured value)	k	0.94

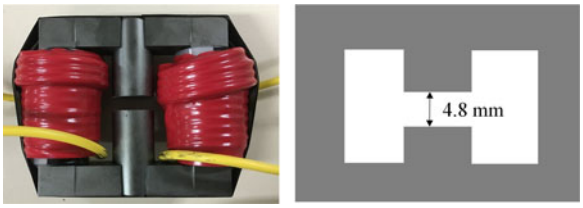

Fig. 20. Prototype of the coupled inductor without air gap in the outer legs (Conventional design method).

V. CONFIRMATION OF THE VALIDITY OF THE PROPOSED DESIGN METHOD UNDER THE DC-BIASED MAGNETIZATION CONDITION

A. Simulation Results

In order to show the effectiveness of the proposed design method over the conventional one [27], a multiphase interleaved boost converter with LCI was simulated. Two simulation case studies are performed using PLECS (Plexim Inc.) simulation software. As a simulation condition, a linear analysis is utilized. In other words, magnetic saturation, or variation of the values of the magnetic reluctances depending on magnetic field intensity, is not considered.

1) LCI designed by the proposed design method: Fig. 21(a) shows inductor currents in each phase and magnetic flux waveforms of LCI designed by the proposed design method under conditions specified in Table I. The designed magnetic parameters are ($R_{\mathrm{mo}} =$ 0.93 A/μWb, $R_{\mathrm{mc}} =$ 4.66 A/μWb, $N =$ 21 turns). As can be seen in Fig. 21(a), the inductor currents satisfy both the designed inductor ripple current of 3 A and inductor average currents with the unbalanced factor $\delta =$ 0.05. From the magnetic flux waveforms, the peak flux Φ_{op1} in the outer leg is 44.9 μWb. The flux density is calculated as 244 mT. Therefore, the validity of the proposed method was confirmed.
2) LCI designed by the conventional design method [27]: Fig. 21(b) shows inductor currents in each phase and magnetic flux waveforms under conditions given in Table I using the designed magnetic parameters ($R_{\mathrm{mo}} =$ 0.18 A/μWb, $R_{\mathrm{mc}} =$ 2.89 A/μWb, $N =$ 14 turns). As can be seen in Fig. 21(b), the peak flux Φ_{op1} is much greater than the designed magnetic flux because the conventional design method does not take into account the dc-biased magnetization. The flux density is calculated as 451 mT, which is equal to the saturation value of flux density in the ferrite. Therefore, the reliability of the conventional design method is worse than the proposed design method.

The simulation results agree with the analysis carried out in the previous sections. The proposed design method improves the immunity to the unbalanced inductor currents, and minimizes the effect of dc-biased magnetization, which is not considered in the conventional LCI design method.

B. Experimental Results

In this section, the experimental results are presented. This experimental evaluation is conducted under both balanced ($\delta = 0$) and unbalanced inductor currents ($\delta =$ 0.05). The experimental results of the two prototypes are given as follows.

1) LCI designed by the proposed design method: Fig. 22(a) and (b) shows the inductor currents under balanced and unbalanced conditions, respectively. The values of the inductor ripple currents are 2.97 A and 2.98 A, and they almost agree with the designed value of 3 A. It is clear that the magnetic core has not saturated under both balanced and unbalanced conditions. In the case of magnetic saturation, the inductor ripple current increases significantly as the inductance value decreases. The experimental waveforms show a linear behavior under both current balance ($\delta = 0$) and current unbalance ($\delta =$ 0.05) conditions.
2) LCI designed by the conventional design method [27]: Fig. 23(a) and (b) shows the inductor currents under balanced and unbalanced conditions, respectively. The values of the inductor ripple currents are 2.98 A, and they almost agree with the designed value of 3 A under the balanced condition ($\delta = 0$). However, under unbalanced current condition ($\delta =$ 0.05), it can be noticed that the magnetic core is saturated. The values of the inductor ripple currents are 4.5 and 3 A. This condition occurs because no air gap is inserted in the outer legs, so a high value of the coupling factor helps the dc-biased magnetization to increase leading to core saturation. Therefore, LCI without air gaps in the outer legs or with a lower magnetic reluctance R_{mo} is required in advanced control schemes such as high precision current sensors for measuring inductor average current.

C. Evaluation of the Proposed Design Method With Optimal Coupling Coefficient

Finally, the features of the proposed design method are stated. Table VII summarizes the pros and cons of the proposed design method alongside other inductor design methods. The design examples of core size are also shown in this table to indicate the downsizing effect by using the proposed design method with the optimal value of k. From this table, both high immunity to unbalanced current and downsizing magnetic components can be realized by using the proposed design method with the optimal k.

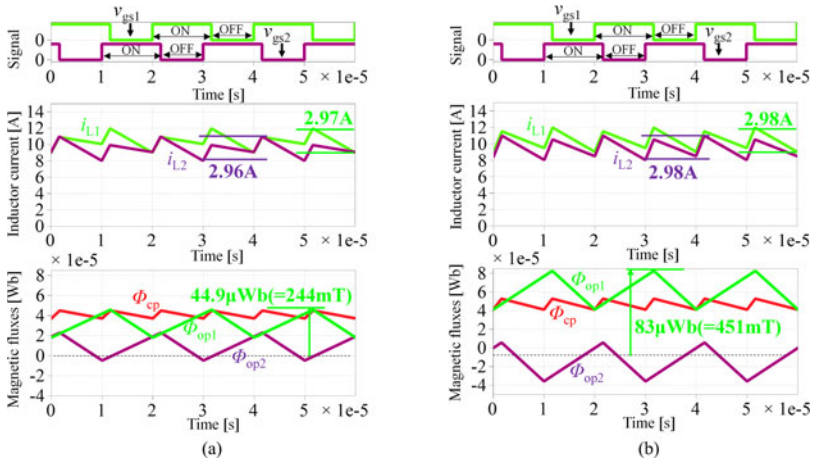

Fig. 21. Simulation waveforms based on the proposed and conventional design methods under the $\delta = 0.05$ condition. (a) Proposed design method. (b) Conventional design method.

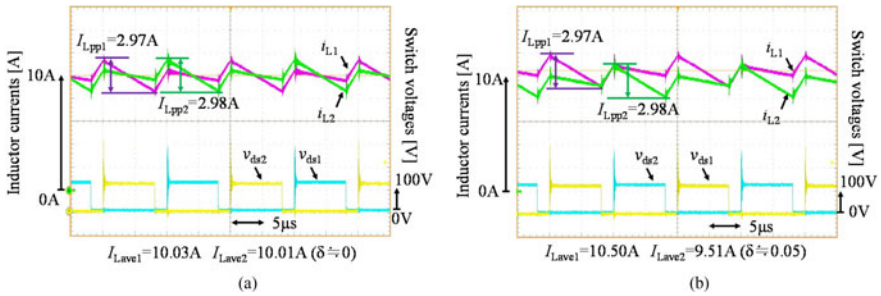

Fig. 22. Experimental current waveforms of the LCI designed by the proposed design method. (a) Balanced condition. (b) Unbalanced condition.

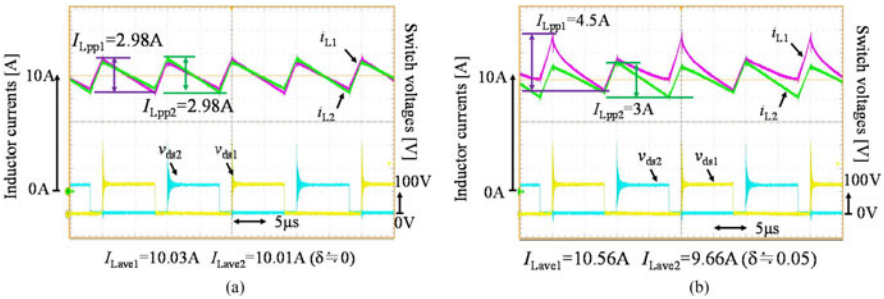

Fig. 23. Experimental current waveforms of the LCI designed by the conventional design method. (a) Balanced condition. (b) Unbalanced condition.

TABLE VII
FEATURES OF EACH DESIGN METHOD AND CORE VOLUME COMPARISON

	Loosely Coupled Inductor (LCI)			Non-coupled inductors
	Proposed design method with the optimal k	Proposed design method with the lower or higher k than the optimal k	Conventional design method without air gap in outer leg[27]	
Immunity to unbalanced currents	High	High	Very low	Not applicable
Core or winding volumes	Small	Large	Very small	Very large
Core volume comparison results				
Evaluation conditions	TABLE I (Note that only duty ratio is changed from 0.583 to 0.75 to confirm the effectiveness of the optimal k), TABLE II			
Number of turns	N: 30turns (each phase)			
Winding area	A_w : 126mm^2			
Magnetic reluctance values	R_{mo}: 1.30 A/μWb R_{mc}: 3.45 A/μWb (derived from (12))	R_{mo}: 0.314 A/μWb R_{mc}: 4.92 A/μWb (derived from (12))	R_{mo}: 0.152 A/μWb R_{mc}: 5.17 A/μWb (the design method are shown in [27])	R_m: 3.6 A/μWb (R_m is the magnetic reluctance of the closed magnetic path in the core)
Coupling coefficient	k: 0.73 (the optimal value derived from (22) and (10))	k: 0.94 (a provisional value)	k: 0.97 (derived from (10))	Not applicable
Inductance values	L_{lk}: 110 μH M: 292 μH (derived from (9))	L_{lk}: 88 μH M: 1.39 mH (derived from (9))	L_{lk}: 86 μH M: 2.92 mH (derived from (9))	L_{self}: 250 μH
Sectional area of the core	A_o: 242 mm^2 A_c: 326 mm^2 (derived from (24))	A_o: 358 mm^2 A_c: 269 mm^2 (derived from (24))	A_o: 164 mm^2 A_c: 262 mm^2 (the design method are shown in [27])	A_{non}: 400 mm^2 (derived from (15) and (2))
Core volume	$Vol_{coupled}$: 0.045 liter (derived from (16))	$Vol_{coupled}$: 0.065 liter (derived from (16))	$Vol_{coupled}$: 0.029 liter (derived from (16))	Vol_{total_non}: 0.099 liter (derived from (18))

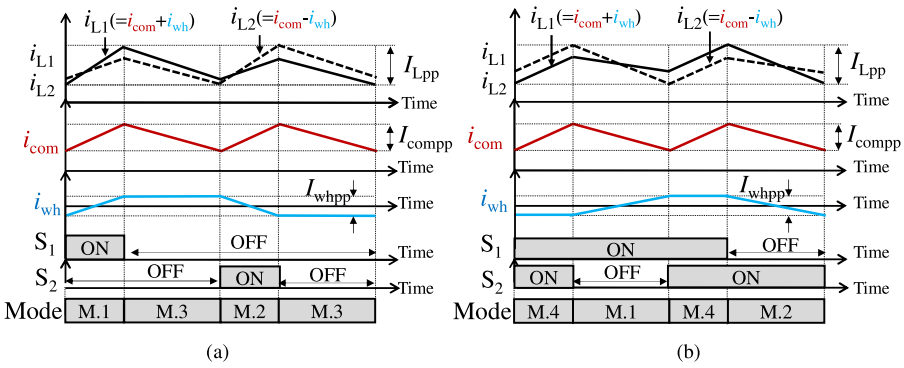

Fig. 24. Inductor current waveforms for duty ratio less or greater than 0.5. (a) $d \leq 0.5$. (b) $d > 0.5$.

VI. Conclusion

This paper proposed a magnetic design method of integrating magnetic components to overcome the magnetic saturation that arises from unbalanced inductor currents in interleaved multiphase boost converters. The proposed design method is especially useful for practical designs. We obtain the following information for integrated magnetic components used in interleaved boost converters.

1) On the basis of the analysis results of Section III, when an unbalanced average current flows into the windings of the LCI with a higher coupling coefficient, the peak flux in the outer leg of LCI increases considerably, causing magnetic saturation. When magnetic saturation is avoided in a state where a high coupling coefficient is maintained, the downsizing effect of the LCI is reduced in comparison with noncoupled inductors. However, when the coupling coefficient is optimized based on the maximum permissible percentage of unbalanced inductor average currents, LCI can be downsized. These results are given in Sections IV and V.
2) The design and implementation methods were proposed in Section IV. The validity of the design and implementation methods is confirmed from the simulation and experimental tests in Section V. By using the proposed design method, high immunity to unbalanced inductor current within the range of the designed δ can be realized, while maintaining the downsizing effect of LCI.

Therefore, this design method can enhance the reliability of integrated magnetic components in interleaved converters. Although the validity of the proposed design method was confirmed by using ferrite cores, the proposed design method is especially effective for high-permeability magnetic materials such as nanocrystalline, amorphous, and Si-steel cores.

Appendix

I. Analysis of Inductor Ripple Currents

In this section, the current ripple analysis is conducted to clarify the relationship between each inductance and inductor ripple current. Fig. 24(a) and (b) illustrates the inductor current waveforms for duty ratio less and greater than 0.5, respectively.

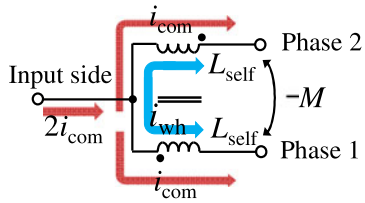

Fig. 25. Current paths of each current components.

Note that these waveforms are drawn under the balanced inductor average current condition. In the two-phase interleaved boost converter, there are four operation modes and these operation modes differ for duty ratio less and greater than 0.5. The relationships between the applied voltages to the inductor windings and inductor ripple currents of each phase are given by

$$v_{L1} = L_{\rm self}\frac{i_{L1}}{dt} - M\frac{di_{L2}}{dt}, \quad v_{L2} = L_{\rm self}\frac{i_{L2}}{dt} - M\frac{di_{L1}}{dt} \tag{26}$$

where v_{L1} and v_{L2} are the applied voltages to inductor windings in each phase, and v_{L1} and v_{L2} equal V_i under the on-state condition, and equal $V_i - V_o$ under the off-state condition. The current ripple analysis results for each operation modes are summarized in Table VII. As can be seen in Table VII, the inductor currents i_{L1}, i_{L2} can be separated into a common current $i_{\rm com}$ and a wheeling current $i_{\rm wh}$, and their current paths are shown in Fig. 25. The inductor ripple current equations including both the common and wheeling current components are summarized in Table IX. The slope of $i_{\rm com}$ changes every time the operation mode changes. Based on (31) and (33), the leakage inductance $L_{\rm lk} = L_{\rm self}$–$M$ decides the amplitude of common ripple current. On the other hand, the slope of $i_{\rm wh}$ changes only during modes 1 and 2 because no voltage is applied to the transformer of LCI during modes 3 and 4. If the value of mutual inductance is high, the wheeling ripple current decreases dramatically. In the case of the noncoupled inductor, the inductor ripple current usually increases as long as the switch S_1 is turned ON. On the other hand, if LCI has high mutual inductance, the inductor ripple current of LCI decreases even if the switch S1 is turned ON. Therefore, in the case of the LCI, the inductor ripples can be effectively reduced in comparison with the noncoupled inductor, which is considered as one of the advantages of the employing integrated magnetics.

TABLE VIII
ANALYSIS RESULTS OF THE RELATIONSHIP BETWEEN EACH INDUCTANCE AND INDUCTOR CURRENT

Mode1 (S_1 : ON, S_2 : OFF)		Mode2 (S_1 : OFF, S_2 : ON)	
$\begin{cases} \frac{di_{L1\_mod1}}{dt} = \frac{1}{(L_{self}-M)} \cdot (V_i - \frac{1}{2}V_o) + \frac{1}{(L_{self}+M)} \cdot \frac{1}{2}V_o \\ \frac{di_{L2\_mod1}}{dt} = \frac{1}{(L_{self}-M)} \cdot (V_i - \frac{1}{2}V_o) - \frac{1}{(L_{self}+M)} \cdot \frac{1}{2}V_o \end{cases}$	(27)	$\begin{cases} \frac{di_{L1\_mod2}}{dt} = \frac{1}{(L_{self}-M)} \cdot (V_i - \frac{1}{2}V_o) - \frac{1}{(L_{self}+M)} \cdot \frac{1}{2}V_o \\ \frac{di_{L2\_mod2}}{dt} = \frac{1}{(L_{self}-M)} \cdot (V_i - \frac{1}{2}V_o) + \frac{1}{(L_{self}+M)} \cdot \frac{1}{2}V_o \end{cases}$	(28)
Mode3 (S_1 : OFF, S_2 : OFF)		Mode4 (S_1 : ON, S_2 : ON)	
$\frac{di_{L1\_mod3}}{dt} = \frac{di_{L2\_mod3}}{dt} = \frac{1}{(L_{self}-M)} \cdot (V_i - V_o)$	(29)	$\frac{di_{L1\_mod4}}{dt} = \frac{di_{L2\_mod4}}{dt} = \frac{1}{(L_{self}-M)} \cdot V_i$	(30)

TABLE IX
INDUCTOR RIPPLE CURRENT EQUATIONS INCLUDING ITS CURRENT COMPONETS

Duty ratio	Common ripple current		Wheeling ripple current		Inductor current ripple	
$d \le 0.5$	$I_{compp} = \frac{1}{L_{self}-M} \cdot (V_i - \frac{V_o}{2}) \cdot d \cdot T_s$	(31)	$I_{whpp} = \frac{1}{L_{self}+M} \cdot \frac{V_o}{2} \cdot d \cdot T_s$	(32)	$I_{Lpp} = I_{compp} + I_{whpp}$	(35)
$d > 0.5$	$I_{compp} = \frac{1}{L_{self}-M} \cdot (\frac{V_o}{2} - V_i) \cdot (1-d) \cdot T_s$	(33)	$I_{whpp} = \frac{1}{L_{self}+M} \cdot \frac{V_o}{2} \cdot (1-d) \cdot T_s$	(34)		

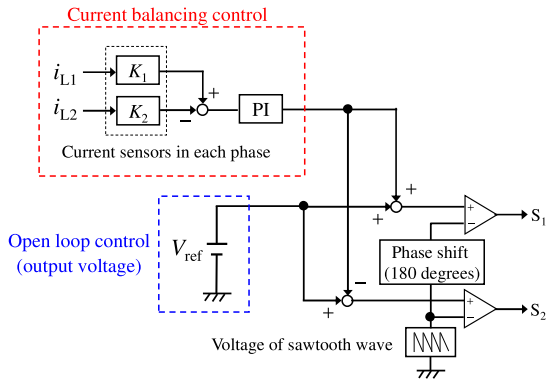

Fig. 26. Control block of interleaved converter for inductor current balancing control.

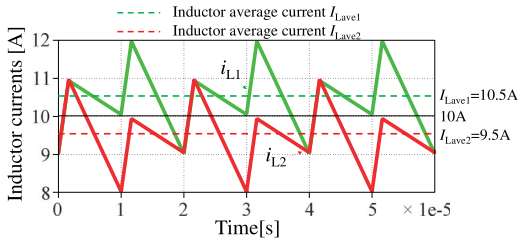

Fig. 27. Inductor current waveforms.

If a positively coupled inductor with $+M$ (not $-M$) is used, although the common ripple current can be reduced effectively, the wheeling ripple current is increased. In addition, the dc flux cancellation would not be obtained in this case, because the dc fluxes generated by each phase average current are added together on the transformer magnetic path.

II. Relationship Between the Unbalanced Inductor Current and Unbalanced Current Sensor Gains

This section introduces the relationship between the gain errors of the current sensors in each phase and the unbalanced average currents. The interleaved converter usually employs a current balancing control. One of the examples of current balancing control is shown in Fig. 26. In this control block, the output voltage feedback loop is omitted for simplicity, and it is shown as an open-loop control. This current balancing control has a Proportional-Integral (PI) compensator with a long integrating time as compared with the switching period of S_1 and S_2 in order to eliminate the influence of inductor ripple currents. Then, the output signal of the PI compensator, which shows an integrated difference between the inductor average current in each phase, is the input to the voltage control signal through the adder or subtractor. In other words, by slightly modulating the pulse width of PWM signals in each phase, the inductor average currents in each phase are balanced. Then, in order to investigate this relationship, a simulated evaluation is conducted. The circuit parameters for evaluation are the same as Table I. The current sensor gains in each phase are $K_1 = 0.095$ and $K_2 = 0.105$, respectively. These values have a tolerance (or an error) of $\delta = \pm 5\%$ from the average gain K_{ave} $(= (K_1 + K_2)/2)$, and the relationship is shown as follows:

$$\begin{cases} K_1 = K_{ave}\,(1 \mp \delta) \\ K_2 = K_{ave}\,(1 \pm \delta)\,. \end{cases} \tag{36}$$

The reference voltage V_{ref} is set as 0.583, and the peak-to-peak amplitude of the saw tooth voltage is 1 V. On the other hand, the transfer function of PI compensator is as follows:

$$G_{PI}\,(s) = K_p + \frac{K_p}{sT_i} \tag{37}$$

where K_p is the proportional gain and T_i is the integrating time. In this simulation, K_p and T_i are set at 0.001 and 100 μs, respectively, as five times the switching period. The magnetic parameters of LCI are used in the design values shown in Table III. By using these conditions, the simulated evaluation was carried out. The inductor current waveforms are shown in Fig. 27. From this figure, the unbalanced ratio of the inductor average current to complete balanced condition is identical to the unbalanced gains of current sensors. Therefore, the gain er-

rors of the current sensors in each phase and the unbalanced average currents are summarized as follows:

$$I_{\mathrm{Lave1}} = \frac{K_2}{K_{\mathrm{ave}}} = \frac{K_{\mathrm{ave}}\,(1 \pm \delta)}{K_{\mathrm{ave}}} = 1 \pm \delta$$
$$I_{\mathrm{Lave2}} = \frac{K_1}{K_{\mathrm{ave}}} = \frac{K_{\mathrm{ave}}\,(1 \mp \delta)}{K_{\mathrm{ave}}} = 1 \mp \delta. \qquad (38)$$

These relationships are helpful in deciding the maximum permissible percentage of the practical design of LCI as a reference.

REFERENCES

[1] M. Kuypers, "Application of 48 volt for mild hybrid vehicles and high power loads," SAE Int., Warrendale, PA, USA, SAE Tech. Paper, 2014-01-1790, Apr. 2014.

[2] Y. Hasuke, H. Sekine, K. Katano, and Y. Nonobe, "Development of Boost Converter for MIRAI," SAE Int., Warrendale, PA, USA, SAE Tech. Paper, 2015-01-1170, Apr. 2015.

[3] M. Hirakawa, M. Nagano, Y. Watanabe, K. Andoh, S. Nakatomi, and S. Hashino, "High power density DC/DC converter using the close-coupled inductors," in *Proc. IEEE Energy Convers. Congr. Expo.,* Sep. 2009, pp. 1760–1767.

[4] M. Pavlovsky´, G. Guidi, and A. Kawamura, "Assessment of coupled and independent phase designs of interleaved multiphase buck/boost DC–DC converter for EV power train," *IEEE Trans. Power Electron.*, vol. 29, no. 6, pp. 2693–2704, Jun. 2014.

[5] K. J. Hartnett, J. G. Hayes, M. G. Egan, and M. S. Rylko, "CCTT-Core split-winding integrated magnetic for high-power DC–DC converters," *IEEE Trans. Power Electron.*, vol. 28, no. 11, Nov. 2013, pp. 4970–4984,

[6] E. A. Burton, G. Schrom, F. Paillet, J. Douglas, W. J. Lambert, K. Radhakrishnan, and M. J. Hill, "FIVR—Fully integrated voltage regulators on 4th generation Intel Core SoCs," in *Proc. IEEE Appl. Power Electron. Conf. Expo.*, Mar. 2014, pp. 432–439.

[7] Q. Li, Y. Dong, F. C. Lee, and D. J. Gilham, "High-density low-profile coupled inductor design for integrated point-of-load converters," *IEEE Trans. Power Electron.*, vol. 28, no. 1, pp. 547–554. Jan. 2012.

[8] J. Imaoka *et al.*, "Feasible evaluations of coupled multilayered chip inductor for POL converters," *IEEJ J. Ind. App.*, vol. 4, no. 3, pp. 126–135. May 2015.

[9] K. J. Hartnett, J. G. Hayes, M. G. Egan, M. S. Rylko, B. J. Barry, and J. W. Masłoń, "Comparison of 8-kW CCTT IM and discrete inductor interleaved boost converter for renewable energy applications," *IEEE Trans. Ind. App.*, vol. 51, no. 3, pp. 2455–2469, May 2015.

[10] K. Tseng and C. Huang, "High step-up high-efficiency interleaved converter with voltage multiplier module for renewable energy system," *IEEE Trans. Ind. Electron.*, vol. 61, no. 3, pp. 1311–1319, Mar. 2014.

[11] L. Meyer and B. Bras, "Rare earth metal recycling," in *Proc. IEEE Int. Symp. Sustain. Syst. Technol.*, May 2011, pp. 1–6,

[12] L. Gaines, "The future of automotive lithium-ion battery recycling: Charting a sustainable course," *Sustain. Mater. Technol.*, vols. 1/2, pp. 2–7, Dec. 2014.

[13] National Institute for Materials Science, Tsukuba, Japan, "The wall of resource constraints worldwide by 2050," (in Japanese), Feb. 2007. [Online]. Available: http://www.nims. go.jp/news/press/2007/02/200702150/p200702150.pdf

[14] J. W. Kolar, J. Biela, and J. Miniböck, "Exploring the pareto front of multi-objective single-phase PFC rectifier design optimization –99.2% efficiency vs. 7 kW/dm^3 power density," in *Proc. IEEE 6th Int. Power Electron. Motion Control Conf.*, May 2009, pp. 1–21

[15] J. Imaoka, M. Yamamoto, Y. Nakamura, and T. Kawashima, "Analysis of output capacitor voltage ripple in multi-phase transformer-linked boost chopper circuit," *IEEJ J. Ind. App.*, vol. 2 no. 5 pp. 252–260, Sep. 2013.

[16] P. Zumel, O. García, J. A. Oliver, and J. A. Cobos, "Differential-mode EMI reduction in a multiphase DCM flyback converter," *IEEE Trans. Power Electorn.*, vol. 24, no. 8, pp. 2013–2020, Aug. 2009.

[17] K. Mainali and R. Oruganti, "Conducted EMI mitigation techniques for switch-mode power converters: A survey," *IEEE Trans. Power Electron.*, vol. 25, no. 9, pp. 2344–2356, Sep. 2010.

[18] C. Wang, M. Xu, F. C. Lee, and B. Lu, "EMI study for the interleaved multi-channel PFC," in *Proc. IEEE Power Electron. Specialists Conf.*, Jul. 2007, pp. 1336–1342.

[19] T. Qian and B. Lehman, "Coupled input-series and output-parallel dual interleaved flyback converter for high input voltage application," *IEEE Trans. Power Electron.*, vol. 23, no. 1, pp. 88–95, Feb. 2008.

[20] F. Forest, E. Labouré, T. A. Meynard, and J. Huselstein, "Multicell interleaved flyback using intercell transformers," *IEEE Trans. Power Electron.*, vol. 22, no. 5, pp. 1662–1671, Sep. 2007.

[21] L. Wong, Y. Lee, D. K. Cheng, and M. H. L. Chow, "Two-phase forward converter using an integrated magnetic component," *IEEE Trans. Aerospace Electron. Sys.*, vol. 40, no. 4, pp. 1294–1310, Sep. 2004.

[22] Y. Su, D. Hou, F. C. Lee, and Q. Li, "Low profile coupled inductor substrate with fast transient response," in *Proc. IEEE Applied Power Electron. Conf. Expo.,*, Mar. 2015. pp. 1161–1168.

[23] P-L Wong, F. C. Lee, P. Xu, and K. Yao, "Critical inductance in voltage regulator modules," *IEEE Trans. Power Electron.*, vol. 17, no. 4, pp. 485–492. Aug. 2002.

[24] P. Wong, P. Xu, B. Yang, and F. C. Lee, "Performance improvements of interleaving VRMs with coupling inductors," *IEEE Trans. Power Electron.*, vol. 16, no. 4, pp. 499–507, Jul. 2001.

[25] W. Huang and B. Lehman, "A compact coupled inductor for interleaved multiphase DC–DC converters," *IEEE Trans. Power Electron.*, vol. 31, no. 10, pp. 6770–6775, Oct. 2016.

[26] J. Imaoka, S. Kimura, W. Martinez, and M. Yamamoto, "A novel integrated magnetic core structure suitable for transformer-linked interleaved boost chopper circuit," *IEEJ J. Ind. App.*, vol. 3, no. 5, pp. 395–404, Sep. 2014.

[27] S. Kimura, Y. Itoh, W. Martinez, M. Yamamoto, and J. Imaoka, "Downsizing effects of integrated magnetic components in high power density DC–DC converters for EV and HEV applications," *IEEE Trans. Ind. App.*, vol. 52, no. 4, pp. 3294–3305, Jul. 2016.

[28] H. Kosai, S. McNeal, B. Jordan, J. Scofield, B. Ray, and Z.Turgut, "Coupled inductor characterization for a high performance interleaved boost converter," *IEEE Trans. Magn.*, vol. 45, no. 10, pp. 4812–4815. Oct. 2009.

[29] K. Umetani, J. Imaoka, M. Yamamoto, S. Arimura, and T. Hirano, "Evaluation of the Lagrangian method for deriving equivalent circuits of integrated magnetic components: A case study using the integrated winding coupled inductor," *IEEE Trans. Ind. App.*, vol. 51, no. 1, pp. 547–555, Jun. 2015.

[30] W. Huang and J. A. A. Qahouq, "Input voltage ripple-based sensorless current sharing autotuning controller for multiphase DC–DC converters," *IEEE Trans. Ind. App.*, vol. 52, no. 5, pp. 4117–4125. Sep. 2016.

[31] H. Kim, M. Falahi, T. M. Jahns, and M. W. Degner, "Inductor current measurement and regulation using a single DC link current sensor for interleaved DC–DC converters," *IEEE Trans. Power Electron.*, vol. 26, no. 5, pp. 1503–1510, May 2011.

[32] H-C. Chen, C-Y Lu, and L-M Huang, "Decoupled current-balancing control with single-sensor sampling-current strategy for two-phase interleaved boost-type converters," *IEEE Trans. Ind. Electron.*, vol. 63, no. 3, pp. 1507–1518. Mar. 2016.

[33] M. Gleissner and Mark-M. Bakran, "Influence of inverse coupled inductors on fault-tolerant operation of two-phase DC-DC converters," in *Proc. 13th Eur. Conf. Power Electron. Appl.,* Sep. 2015. pp. 1–11.

[34] Y. Itoh, F. Hattori, S. Kimura, J. Imaoka, and M. Yamamoto, "Design method considering magnetic saturation issue of coupled inductor in interleaved CCM boost PFC converter," in *Proc. IEEE Energy Convers. Congr. Expo.*, Sep. 2015, pp. 2616–2621.

[35] W. Colonel and T. McLyman, *Transformer and Inductor Design Handbook*. New York, NY, USA: Marcel Dekker, 2004.

[36] M. Olszewski, "Evaluation of the 2010 Toyota Prius hybrid synergy drive system," Oak Ridge Nat. Lab., Oak Ridge, TN, USA, Mar. 2011. Tech. Rep. ORNL/TM-2010/253, [Online]. Available: http://info.ornl.gov/sites/publications/files/pub26762.pdf

[37] TDK Corporation, 2017. [Online]. Available: https://product.tdk.com/info/en/products/index.html

[38] LEM, 2017. [Online]. Available: http://www.lem.com/hq/en/content/view/28/104/

Jun Imaoka (S'11–M'15) received the M.S. and Ph.D. degrees in electronic function and system engineering from Shimane University, Matsue, Japan, in 2013 and 2015, respectively.

Since October 2015, he has been at Kyushu University, Fukuoka, Japan, as an Assistant Professor. His research interests include design of integrated magnetic components, modeling for high power density power converters, thermal management for power converters, magnetic material application, EMI of switching power supply.

Kenkichiro Okamoto received the B.S. degree in electrical and electronic engineering from Yamaguchi University, Yamaguchi, Japan, in 2016. He is currently working toward the M.S. degree in electrical engineering at Kyushu University, Fukuoka, Japan.

His current research focuses on the design of magnetic components for dc/dc converter.

Shota Kimura (S'13) received the B.S. and M.S. degrees in electrical and electronic system engineering from Shimane University, Shimane, Japan, in 2013 and 2015, respectively. Since 2015, he has been working toward the Ph.D. degree in mechanical/electronic engineering and information systems at Shimane University, Shimane, Japan.

His research interests include design of integrated magnetic components for high power density dc–dc converter.

Mostafa Noah (S'15) received the B.Sc. and M.Sc. degrees in electrical engineering from Cairo University, Giza, Egypt, in 2009 and 2014, respectively. He is currently working toward the Ph.D. degree in electronic function and system engineering from Shimane University, Matsue, Japan.

From 2009–2015, he also was in the multinational consultant Dar Al-Handasah and SCG as an electrical design engineer, where he was responsible for designing the electrical system for mega projects. His research interests include dc/dc converters, design of integrated magnetics, and transformer design for *LLC* resonant converter.

Wilmar Martinez (S'09–M'16) received the B.S. degree in electronics engineering and the M.Sc. degree in electrical engineering from Universidad Nacional de Colombia, Bogotá, Colombia, in 2011 and 2013, respectively, and the Ph.D. degree in electronic function and system engineering from Shimane University, Matsue, Japan, in 2016.

He is currently in the Toyota Technological Institute, Nagoya, Japan. His research interests include multiobjective optimization of power converters, evaluation of iron losses at high carrier frequency in electric motors, and high power density converters for electric vehicles and renewable energies.

Masayoshi Yamamoto (M'11) received the M.S. and Ph.D. degrees in science and engineering from Yamaguchi University, Yamaguchi, Japan, in 2000 and 2004, respectively.

From 2004 to 2005, he was with Sanken Electric Company, Ltd., Saitama, Japan. From 2006 to 2017, he was in the Interdisciplinary Faculty of Science and Engineering, Shimane University, Matsue, Japan, as an Associate Professor. He is currently a Professor in the Institute of Materials and Systems for Sustainability, Nagoya University, Nagoya, Japan. His research interests include power supply for HEV (boost converter, buck converter, three-phase inverter, digital control), charging system for EV, LED illumination system for a tunnel, EMI of switching power supply, and wireless power transfer.

Masahito Shoyama (M'93–SM'06) received the B.S. degree in electrical engineering and the Dr. Eng. degree in electrical engineering from Kyushu University, Fukuoka, Japan, in 1981 and 1986, respectively.

In 1986, he joined the Department of Electronics, Kyushu University, as a Research Associate. He has been an Associate Professor since 1990, and a Professor since 2010. Since 2009, he has been in the Department of Electrical Engineering, Faculty of Information Science and Electrical Engineering, Kyushu University. He has been active in the field of power electronics, especially in the areas of bidirectional converters for dc/ac power systems, high-frequency switching converters for renewable energy sources, power factor correction converters, and electromagnetic compatibility.